Solar Energy 241 (2022) 220–230

Contents lists available at ScienceDirect

Solar Energy

journal homepage: www.elsevier.com/locate/solener

Investigation of collector flow for 1:30 scale solar chimney power plant model

M.K. Hasan [a,*], A. Gross [a], L. Bahrainirad [b], H.F. Fasel [b]

[a] Department of Mechanical and Aerospace Engineering, New Mexico State University, Las Cruces, 88003, NM, USA
[b] Department of Aerospace and Mechanical Engineering, University of Arizona, Tucson, 85721, AZ, USA

ARTICLE INFO

Keywords:
Solar chimney power plant
Scaled model experiment
Buoyancy-driven instability
Rayleigh-Bénard-Poiseuille flow
Numerical stability analysis

ABSTRACT

Investigations of the flow field in scaled solar chimney power plant model were carried out using a two pronged approach: Experiments were carried out for a 1:30 scale model of the Manzanares solar chimney power and accompanying numerical simulations. Emphasis was on investigating the hydrodynamic stability of developing inward radial Rayleigh-Bénard-Poiseuille flow under the collector of the 1:30 scale model. Temperature measurements under the collector of the model provided the reference data for comparison with results from a direct numerical simulation. The simulation results reveal that both steady longitudinal (streamwise) modes and unsteady oblique disturbance waves are amplified. Steady longitudinal modes with an azimuthal wavelength of approximately 1.5 times half-height of the collector exhibit the strongest spatial growth. Towards the collector outflow (or inflow to the chimney), the steady modes appear to merge and the growth rates are attenuated as a result of the strong streamwise flow acceleration. A scaling analysis suggests that the present results are relevant for the design and operation of realistic large-scale solar chimney power plants. Based on the present investigation, buoyancy-driven instability and coherent longitudinal flow structures are to be expected for full-size solar chimney power plants. The coherent flow structures will affect the heat transfer and total pressure losses in the collector.

1. Introduction

Solar chimney power plants (SCPPs) are attractive because they offer to generate clean renewable energy at an affordable cost and without resorting to high-tech materials or fabrication processes. Together with other renewable energy sources, they will help reduce the dependence on fossil fuels and thus address major environmental concerns such as global warming. The two main components of an SCPP are the collector and chimney (Fig. 1). The collector has a circular footprint and a translucent cover. The chimney is located at the center of the collector. The operating principle is simple compared to conventional power plants: As the air under the collector cover is heated by the solar irradiation, it becomes hotter and less dense. The hot air rises in the central chimney as a result of the chimney effect. Turbines at the chimney inlet extract energy from the flow.

The first SCPP was designed and built by Schlaich, Bergermann and Partner in Manzanares, Spain and operated between 1982 to 1989. It produced nearly 50 kW of electrical power (Haaf et al., 1983; Haaf, 1984; Schlaich, 1995; Schlaich et al., 2005). According to Schlaich (1995), the generated electrical power can be estimated from

$$P = \eta_c \eta_t \frac{2}{3} g \frac{H_{ch} \pi r_{coll}^2 I}{c_p T_a}, \tag{1}$$

where η_c and η_t are the collector and turbine efficiency, g is the gravitational acceleration, I is the solar irradiation, c_p is the specific heat capacity, and T_a is the ambient temperature. The generated power scales with the collector area, πr_{coll}^2 and the chimney height, H_{ch}. Various researchers have pointed out that the turbine pressure drop ratio of 2/3 in Eq. (1) is sub-optimal and suggested the use of values in the range 0.8–0.97 (Bernardes et al., 2003; Backström and Fluri, 2006; Nizetic and Klarin, 2010; Guo et al., 2013).

Physically, the flow inside the collector of solar chimney power plants resembles an inward radial channel flow. The radial channel flow between two horizontal parallel plates with a vertical temperature gradient and opposing gravitational field is known as radial Rayleigh-Bénard-Poiseuille (RBP) flow. For radial RBP flow the streamlines are converging and the flow is accelerating in the radial direction. This is different from conventional plane RBP flow, where the streamlines are parallel and the flow is unaccelerated. Plane RBP flow can be thought

* Corresponding author.
E-mail address: hasanmdkamrul029@gmail.com (M.K. Hasan).

https://doi.org/10.1016/j.solener.2022.05.059
Received 27 February 2022; Received in revised form 5 May 2022; Accepted 28 May 2022
Available online 14 June 2022

Nomenclature

α^*	Thermal diffusivity
α_i	Spatial growth rate
α_r, β	Radial and azimuthal wavenumber
Δt	Computational time step
η_c	Collector efficiency
η_t	Turbine efficiency
γ	Volumetric thermal expansion coefficient
$\hat{u}$	Mode shape
λ_r, λ_θ	Radial and azimuthal wavelength
ν	Kinematic viscosity
ν_T	Turbulent eddy viscosity
ω	Angular frequency
ϕ	Wave angle
ψ	Phase
ρ	Density
ρ_a	Ambient air density
ρ_{ch}	Density at chimney inlet
ρ_{ref}	Reference density
Θ	Computational grid opening angle
A	Amplitude
c	Phase speed in wave propagation direction
c_p	Specific heat capacity
c_s	Streamwise phase speed
d	Chimney diameter
g	Gravitational acceleration
h	Channel/collector height
H_{ch}	Chimney height
I	Solar irradiation
ix, jx, kx	Grid points in the radial, wall-normal, and azimuthal direction
k	Azimuthal mode number
L_{ref}	Reference length
M	Mach number
P	Electrical power
p	Pressure
Pr	Prandtl number
r	local radius
r_1	Inflow radius
r_2	Outflow radius
r_{ch}	Chimney radius
r_{coll}	Collector radius
Ra	Rayleigh number
Ra_c	Critical Rayleigh number
Ra_T	Turbulent Rayleigh number
Re	Reynolds number
Re_c	Critical Reynolds number
Re_h	Reynolds number based on collector height
$Re_{h,T}$	Turbulent Reynolds number based on collector height
s	Streamwise coordinate
T	Temperature
T^*	Total non-dimensional simulation time
T_a	Ambient temperature
T_b	Collector ground temperature
T_t	Collector cover temperature
T_{avg}	Average temperature
T_{ch}	Temperature at chimney inlet
T_{ref}	Reference temperature
u, v, w	Velocities in the wall-normal, radial, and azimuthal direction
u'	disturbance wave ansatz
u_{max}	Maximum velocity
u_{ref}	Reference velocity
v_r	Radial velocity
v_{ch}	Chimney updraft velocity
v_{in}	Collector inflow bulk velocity
z, r, θ	Coordinates in the wall-normal, radial, and azimuthal direction

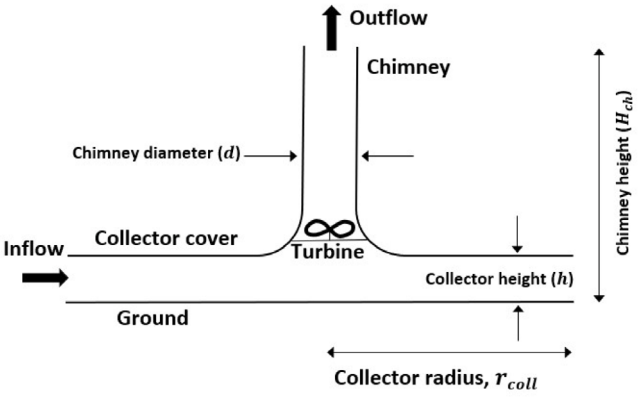

Fig. 1. Schematic showing geometric variables of SCPP.

of as a combination of Rayleigh-Bénard convection and plane Poiseuille flow. Rayleigh-Bénard convection refers to the natural convection in a horizontal layer of fluid that is heated from below. Plane Poiseuille flow refers to the pressure gradient-driven flow between two parallel plates. The buoyancy-driven instability of plane RBP flows has been investigated in great detail. The onset of flow instability is governed by two dimensionless numbers, namely the Reynolds number,

$$Re = \frac{u_{max} h/2}{\nu}, \tag{2}$$

with the maximum velocity, u_{max}, channel height, h, and kinematic viscosity, ν, and the Rayleigh number,

$$Ra = \frac{g h^3 \gamma \Delta T}{\nu \alpha^*}, \tag{3}$$

with volumetric thermal expansion coefficient, γ, temperature difference, ΔT, and thermal diffusivity, α^*. Stability boundaries (neutral curves) for the onset of both buoyancy and viscosity-driven instability of plane RBP flow were provided by Gage and Reid (1968). For $Re < Re_c = 5400$ and $Ra > Ra_c = 1708$, plane RBP flow exhibits buoyancy-driven instability and three-dimensional (3-D) longitudinal waves with a wave angle of 90 degrees are most amplified. When the 3-D waves reach nonlinear amplitudes, longitudinal rolls form. On the other hand, for $Re > Re_c = 5400$ and $Ra < Ra_c = 1,708$, viscosity-driven instability occurs and two-dimensional (2-D) Tollmien-Schlichting (T-S) waves with a wave angle of zero degrees are most amplified. When the 2-D waves reach nonlinear amplitudes, transverse rolls form.

The findings by Gage and Reid (1968) were confirmed by stability analyses and a large number of experimental and numerical investigations. Pearlstein (1985) employed linear stability theory (LST) to investigate the stability of plane RBP flow and discovered that the most critical disturbance waves are either 2-D transverse or 3-D longitudinal. Plane channel flow simulations by Hasan and Gross (2021a) confirmed

the Gage and Reid stability boundaries. A second paper by the same authors discussed a triad interaction of a steady 3-D mode with two unsteady oblique modes (Hasan and Gross, 2020). In plane channel flow experiments, the side walls can change the stability behavior. For example, in finite aspect-ratio RBP flow experiments by Chang et al. (1997) and Chang and Lin (1998), the unstable flow structures developed first near the channel side walls. Luijkx et al. (1981) and Ouazzani et al. (1990) showed that for finite aspect ratio channels, transverse rolls can appear first at low Reynolds numbers while 3-D longitudinal rolls appear first at larger Reynolds numbers. The earlier research suggests that as long as the Rayleigh number is super-critical, the Reynolds number is sub-critical, and when the channel aspect ratio is sufficiently large, longitudinal rolls will develop.

Different from plane channel flow, due to conservation of mass ($\rho v \propto 1/r$-relationship), the flow inside the collector of SCPPs accelerates towards the center (chimney inlet). For boundary layer flows, acceleration is known to be stabilizing (Reed et al., 1996). This suggests that the stability characteristics of inward radial RBP flow in SCPP collectors are different from those of plane RBP flow. Significant differences are especially expected near the collector outlet (or inflow to the chimney) where the acceleration is very large. In addition, different from plane RBP flow, where an infinite number of spanwise wavenumbers is possible, for radial channel flow, the azimuthal wavelengths have to be an integer fraction of the circumference, which varies linearly in the radial direction.

The instability of radial RBP flows has attracted much less attention in the literature than the instability of plane RBP flows. The instability of an outward radial flow between two circular plates was investigated by Van Santen et al. (2000, 2020). For Reynolds numbers between 10 and 50 with $Ra = 2000$, transverse rolls were observed. For $Re = 50$ and $Ra = 5000$, the flow structures became torus-shaped. A large-eddy simulation (LES) of the flow through the collector of a 1:30 scale model of the Manzanares plant by Fasel et al. (2013, 2015) revealed transverse rolls near the inflow and longitudinal rolls in the vicinity of the outflow. Bernardes (2017) carried out a numerical investigation of the inward radial flow between two nearly parallel plates. Longitudinal flow structures developed when the Richardson number exceeded 10. Hasan and Gross (2021b) employed direct numerical simulations (DNS) to investigate the instability of inward radial and spiral RBP flows. The strong streamwise acceleration in particular close to the outflow resulted in a significant decrease of the disturbance growth rates. As for the plane channel flow, both steady longitudinal and unsteady oblique waves were amplified. The steady waves exhibited the highest spatial growth rates.

A large number of publications addresses practical aspects of SCPP design. Reynolds-averaged Navier–Stokes (RANS) calculations by Pastohr et al. (2004) revealed that the efficiency of SCPPs is greatly influenced by the mass flow rate and pressure difference across the collector. Ming et al. (2006, 2008, 2012) employed RANS calculations to investigate the effect of crosswind on the efficiency and performance of SCPPs. The impact of solar radiation and turbine efficiency on the power production and energy losses were studied by Xu et al. (2011). The energy losses exhibited a strong dependence on the mass flow rate. Bernardes et al. (1999) compared various geometries and obtained the largest mass flow rate and outflow temperature for a conical chimney geometry. Numerical analyses by Koonsrisuk and Chitsomboon (2013) focused on the dependence of the generated power on the geometric shape of the different SCPP components. According to their investigation, a combination of a sloping collector roof and a divergent chimney can increase the power output substantially above that for a flat collector and straight chimney. Similarly, Hu et al. (2017) showed that a divergent chimney was more effective than a cylindrical chimney. Ayadi et al. (2017) investigated the effect of the collector roof angle on the performance of a prototype and showed that a negative roof angle increases the flow rate. Ayadi et al. (2018) investigated the chimney height effect on flow rate, temperature increase, and turbulence generation in both experiments and simulations. Fallah and Valipour (2019) found that collector roughness increases the heat transfer and reduces the flow velocity. Experiments and simulations by Nasraoui et al. (2019) revealed that SCPPs with hyperbolic (divergent shape) chimney generate more power than SCPPs with conventional cylindrical chimney, which supports the earlier findings by Koonsrisuk and Chitsomboon (2013). Balijepalli et al. (2020) carried out an uncertainty analysis for different performance parameters such as the flow rate, the maximum turbine pressure drop, and the chimney and overall plant efficiency, for a small scale solar chimney power plant. Khidhir and Atrooshi (2020) enhanced the thermal energy capture by using tracking mirror reflectors. Recently, Bahrainirad et al. (2020) performed measurements inside the collector of a 1:30 scale model of the Manzanares SCPP. This model is situated on the roof of the Aerospace and Mechanical Engineering Department at the University of Arizona. The velocity inside the collector and the temperature in close vicinity of the ground & collector cover were obtained using hotwire anemometers and thermocouples, respectively. This experiment provides the motivation for the present DNS-based numerical stability investigation of the flow through the collector of the 1:30 scale model. The experimental temperature and velocity distributions as well as reference Reynolds and Rayleigh number were matched in the DNS. Based on an analysis of the DNS data, the underlying hydrodynamic instabilities of the inward radial collector flow are identified. The instabilities will determine where coherent flow structures will form. The flow structures will affect the convective mixing and heat transfer and thus have repercussions for the collector effectiveness and total pressure losses. For example, Gentry and Jacobi (2002) showed an increase (over the unperturbed flow) in heat transfer of locally up to 300% for both a flat plate and a channel flow when streamwise vortices were introduced with vortex generators. On average, the heat transfer was increased by 50% while the pressure drop was almost doubled. By increasing the SCPP collector heat transfer, the collector air temperature will be raised, resulting in larger buoyancy forces and higher flow rates. On the other hand, an increased pressure drop will negatively affect the flow rate but also increase the air residence time in the collector which will again improve the heat transfer. This makes the understanding of the instabilities indispensable for the design and safe operation of full-size SCPPs.

This paper is organized as follows: First, a justification for scaled model SCPP experiments and simulations is provided. Then, the experiment and measurements are reviewed. In what follows, the numerical method and the setup of the simulation are described and the procedure for analyzing the time-dependent data is discussed. Next, results form a DNS of the radial RBP flow in the collector for a specific combination of the Reynolds and Rayleigh numbers are presented. The disturbance growth rates, wave angles, phase speeds, and mode shapes obtained from the simulation are analyzed and the implications for full-size SCPP applications are discussed.

2. Scaling analysis

A scaling analysis provides justification for the use of scaled model experiments and simulations for the analysis of full-size SCPPs. Assuming a solar irradiation of $I = 1{,}000\ \mathrm{W/m^2}$, an ambient temperature of $T = 300$ K, a specific heat capacity of $c_p = 1{,}006$ J/(kg K), solar collector thermal efficiency of $\eta_c = 0.5$, and turbine efficiency of $\eta_t = 0.8$ (the assumption is made that the efficiencies do not depend on the SCPP size), the electrical power was estimated from Eq. (1) for three different scales (Table 1). Here, the Manzanares pilot plant (Haaf et al., 1983; Haaf, 1984; Schlaich, 1995; Schlaich et al., 2005) serves as reference (unit scale, 1:1). In practice, for large SCPPs the tower height will likely be capped near 1000 m (to limit construction costs) while the collector area can be increased further. The low conversion efficiency of SCPPs is offset by an estimated low energy production cost for very-large SCPPs.

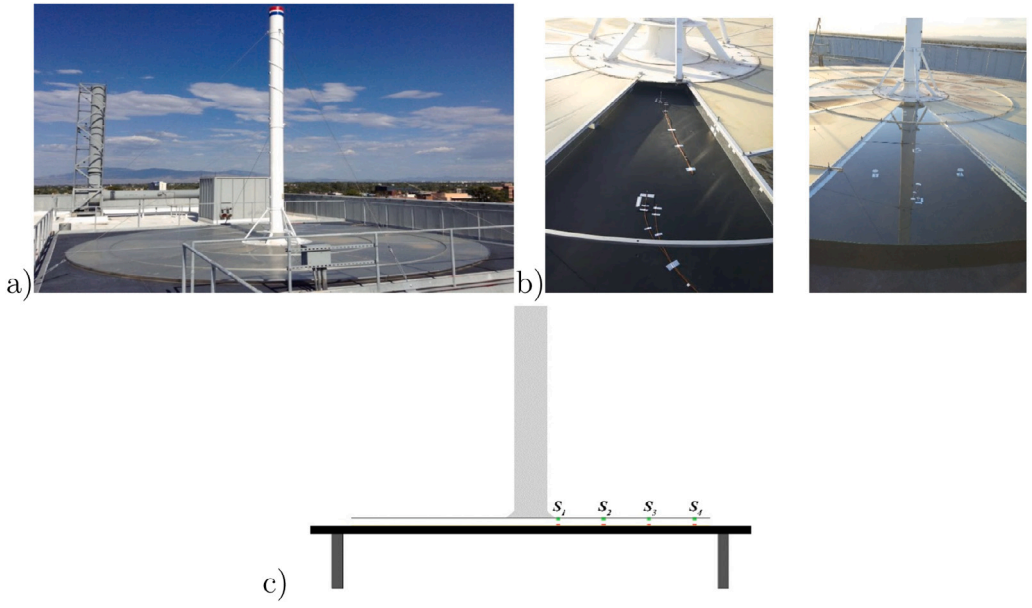

Fig. 2. (a) 1:30 SCPP model, (b) collector section where measurements were taken, and (c) schematic of SCPP model indicating thermocouple locations. *Source:* Reprinted from Bahrainirad et al. (2020).

Table 1
Geometric dimensions and estimated power.

	Collector radius, r_{coll}	Collector height, h	Chimney height, H_{ch}	Chimney diameter, d	Estimated power, P
Model (1:30 scale)	4.07 m	0.067 m	6.6 m	0.33 m	3.0 W
Manzanares (1:1 scale)	122 m	2 m	198 m	10 m	80 kW
Full-size (5:1 scale)	610 m	10 m	990 m	50 m	10 MW

Table 2
Collector at $r/R = 1/6$: Radial velocity, eddy viscosity ratio, as well as laminar and turbulent (subcript "T") Reynolds and Rayleigh numbers.

	v_r	ν_T/ν	Re_h	$Re_{h,T}$	Ra	Ra_T
Model (1:30 scale)	0.8 m/s	24	1,600	65	2.9×10^6	5,000
Manzanares (1:1 scale)	4 m/s	6,000	270,000	44	77×10^9	2,100
Full size (5:1 scale)	6 m/s	50,000	2.0×10^6	40	9.6×10^{12}	3,900

An engineering analysis for a 200 MW plant with 7,000m-diameter collector and 1,000m-high tower by Schlaich et al. (2005) indicated a levelized electricity cost close to 9cent/kWh. With projected costs of 800–1000 million dollars for a single plant and without a solid understanding of the fluid dynamics, power companies and financial institutions are reluctant to commit to this technology.

None of the earlier SCPP investigations have considered the possibility of coherent flow structures in the collector. Such structures will affect both heat transfer and the streamwise pressure drop which is of vital importance for the economics of SCPPs. Based on Reynolds-averaged Navier–Stokes (RANS) calculations for an assumed ground temperature of 350 K (under the collector) (not shown), the approximate Reynolds number (based on collector height, Re_h) and Rayleigh number, Ra, were estimated for the collector at $r/R = 1/6$ (close to the chimney inlet) and are provided in Table 2. An average flow temperature of $T_{av} = 325$ K was assumed for the volumetric thermal expansion coefficient, $\gamma = 1/T_{av}$ (ideal gas, isobaric process). The temperature difference was $\Delta T = 50$ K such that $\gamma\Delta T = 50/325 = 0.15$. Assuming a constant Prandtl number of $Pr = \nu/\alpha = 0.71$, the Rayleigh number can be calculated using $Ra = gh^3\gamma\Delta T/(\nu^2 Pr)$.

The laminar Reynolds and Rayleigh numbers, Re_h and Ra, are increasing of course with the SCPP size (Table 2). However, despite the considerable spread in size, the turbulent dimensionless numbers for the different scales, $Re_{h,T} = \nu/\nu_T \times Re_h$ and $Ra_T = (\nu/\nu_T)^2 \times Ra$, vary by less than factor 2.5. The small variation in the turbulent Reynolds and Rayleigh number suggests that the viscosity- and buoyancy-driven instabilities are similar for the range of scales discussed here. This provides the motivation for the present 1:30 scale experiment and simulation. Instabilities of the laminar flow at the 1:30 model scale will likely manifest themselves as instabilities of the turbulent flow at the full-size scale that will lead to the generation of coherent flow structures.

3. Experiment and measurements

A 1:30 scaled model of the Manzanares SCPP (Haaf et al., 1983; Haaf, 1984; Schlaich, 1995; Schlaich et al., 2005) was designed and built on the roof of the Aerospace and Mechanical Engineering Department at the University of Arizona (Fig. 2a). The radius of the collector inlet and outlet (or, chimney inlet) is $r_{coll} = 4.1$ m and $r_{ch} = 0.15$ m, respectively. The height of the collector is $h = 6.6$ cm. The collector cover consists of 14 pie-slice segments that are held in place by aluminum retainers. The segment over the section where the measurements were taken was made from 0.25 inch thick glass. The other segments were made from plastic green house cover. Hardie-Backer cement boards with a thickness of 0.5 inches were used for the collector base. The cement boards were painted with black acrylic paint. The contoured chimney inlet section was manufactured from fiberglass and matched the scaled geometry of the Manzanares inlet. A fiberglass pipe with an inner diameter of 0.15 m was chosen for the chimney. The chimney height is $H_{ch} = 5.9$ m. Here, it has to be mentioned that the scaled dimensions of the Manzanares plant (Table 1) were only approximately matched to allow for the use of lower-cost prefabricated components (such as the fiberglass pipe). The experimental section of the collector without and with glass cover is exhibited in Fig. 2b. The experimental section was instrumented with eight thermocouples at four radial locations as seen in Fig. 2c.

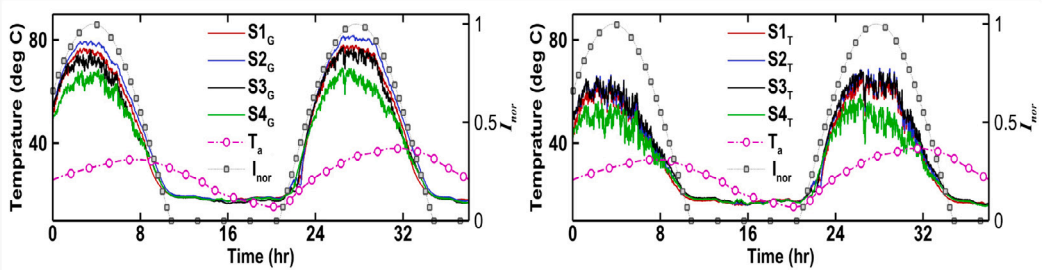

Fig. 3. Time histories for temperature at ground (left) and collector cover (right) as well as ambient temperature and normalized irradiation from 8:40 a.m. on June 13, 2019 to 10:40 p.m. on June 14, 2019.

The radial locations are $r = 3.167$ m for S4 (near collector inflow), $r = 2.278$ m for S3, $r = 2$ m for S2, and $r = 0.5$ m for S1 (near collector outflow). Four of the thermocouples were placed close to the collector cover and the other four thermocouples were placed on the ground. In addition, velocity measurements inside the collector were obtained with a calibrated hotwire anemometer that was mounted on a custom-built traverse.

Time histories of the temperature measurements and the normalized solar irradiation (assuming no obscuration) from 8:40 a.m. on June 13, 2019 to 10:40 p.m. on June 14, 2019 are shown in Fig. 3. The normalized irradiation,

$$I_{nor} = \frac{\sin \Phi}{(sin\Phi)_{maximum}}, \tag{4}$$

was calculated from the sun angle,

$$\Phi = \sin^{-1}(\cos LAT \cos\delta \cos H + \sin LAT \sin\delta) \tag{5}$$

with latitude, LAT, solar declination, $\delta = 23.45 \sin l_c$, and $H = 15(12 - LST)$ (Masters, 2004). The longitude correction, $l_c = 360/365(J_d - 1)$, depends on the Julian day which was $J_d = 164$ for the 13th of June 2019. The local solar time, $LST = [60LT + 4(105 - LONG) + EOT]/60$ is a function of the local time, LT, the longitude, $LONG$, and the equation of time, $EOT = 9.87 \sin 2l_c - 7.53 \cos l_c - 1.5 \sin l_c$. The coordinates of the SCPP are $LAT = 32.2364deg$ and $LONG = -110.95168deg$ and the sunrise and sunset times for June 13th were 5:20 AM and 7:26 PM. The ground heating varied depending on the day and time, cloud cover, wind velocity and direction, and solar irradiation. Fig. 4a provides the measured collector ground and top temperatures for the specified four radial locations averaged in time from 12 p.m. to 4 p.m. on June 14, 2019. Near the inlet ($r \approx 3$ m), a strong increase of both the ground and collector cover temperature is observed. As the outlet is approached, the temperatures drop off slightly. The radial velocity inside the collector for June 14 2pm-3:30pm, as plotted in Fig. 4b, increases in the streamwise direction (from S4 to S1) and decreases in time (as a result of environmental effects such as cloud obscuration). More details on the experiment and the measurements can be found in Bahrainirad et al. (2020).

The averaged measured collector bottom (ground) and top (cover) temperature are $T_b \approx 75$ °C = 348.15 K and $T_t \approx 60$ °C = 333.15 K. The average ambient temperature at the time of the experiment was $T_a \approx 38.4$ °C = 311.55 K. The ambient air density, $\rho_a = 1.132$ kg m^{-3}, was computed from the ideal gas equation assuming an atmospheric pressure of 1 bar. The equation governing the pressure difference between atmosphere and chimney base,

$$\Delta p = \rho_a g H_{ch} \frac{\Delta T}{T_a} = \frac{1}{2}\rho_a v_{ch}^2, \tag{6}$$

was used to estimate the chimney updraft velocity, $v_{ch} \approx 3.28$ m s^{-1}. The air density at the chimney inlet was computed from the ideal gas equation as $\rho_{ch} = 1.035$ kg m^{-3} based on an average temperature of $T_{ch} = (T_t + T_b)/2$ and atmospheric pressure. Based on a control volume analysis between the collector inflow and the chimney outflow,

$$\rho_a 2\pi r_{coll} h v_{in} = \rho_{ch} \pi r_{ch}^2 v_{ch}, \tag{7}$$

the collector inflow bulk velocity, v_{in}, was estimated as 0.124 m s^{-1}. For laminar plane channel flow, the maximum velocity is related to the bulk velocity via $u_{ref} = u_{max} = (3/2)v_{in} = 0.186$ m s^{-1}.

In Fig. 5 the estimated Reynolds and Rayleigh number inside the collector are plotted against the neutral curves for plane RBP flow by Gage and Reid (1968). The Rayleigh number, $Ra = 704,072$, is well above the critical Rayleigh number, $Ra_c = 1,708$. According to Gage and Reid (1968), near the inlet, waves with wave angles between close to zero degrees all the way to 90 degrees are expected to be amplified. Because of continuity, the radial velocity in inward radial RBP flow exhibits an almost hyperbolic dependence on the radius. As the flow accelerates, the Reynolds number increases from 493 to 6983 which is larger than the critical Reynolds number for Tollmien-Schlichting instability to occur in plane channel flow, $Re_c = 5400$.

4. Numerical analysis of collector flow

4.1. Governing equations, discretization, and boundary conditions

The experimental measurements provide the reference conditions for a DNS of the flow through the collector. Different from the experiment, which is exposed to the elements, the simulation is "disturbance-free" and thus allows for an investigation of underlying instabilities. The compressible Navier–Stokes equations in cylindrical coordinates were solved with a compressible Navier–Stokes code by Hasan and Gross (2021b). The u, v, and w velocities are in the wall-normal (z), radial (r), and azimuthal (θ) direction. The convective terms were discretized with fifth-order-accurate upwind- and downwind-biased compact finite differences (Fan, 2016). Fourth-order-accurate compact finite differences were utilized for discretizing the viscous terms (Shukla et al., 2007). The azimuthal derivatives were computed in spectral space. Fast Fourier transforms were employed for the forward and backward transformations from physical to spectral space. A fourth-order-accurate Runge–Kutta method (Fyfe, 1966) was employed for time integration.

The governing equations were made dimensionless by the maximum inflow velocity, $u_{ref} = 0.124$ m s^{-1}, the collector half-height, $L_{ref} = h/2 = 0.033$ m, the average inflow temperature, $T_{ref} = 311.55$ K, and average inflow density, $\rho_{ref} = 1.132$ kg m^{-3}. The reference (i.e., inflow) Reynolds and Rayleigh number (Eqs. (2) and (3)) are 365.90 and 704,072, respectively. Pressure was non-dimensionalized by $\rho_{ref} u_{ref}^2$ and time was made dimensionless by L_{ref}/u_{ref}. The viscosity was obtained from Sutherland's law and normalized by the inflow viscosity. The Boussinesq-approximation was invoked for computing the buoyancy acceleration. The reference Mach and Prandtl number for the simulation were $M = 0.025$ and $Pr = 0.71$.

The bottom and top wall temperature were set to the average measured $T_b = 348.15$ K and $T_t = 333.15$ K. No-slip and no-penetration boundary conditions were enforced at the bottom and top wall (ground and collector cover). The top (collector cover) and bottom wall (collector ground) pressure were computed with one-sided finite differences (Hasan and Gross, 2021a). At the inflow boundary, a parabolic

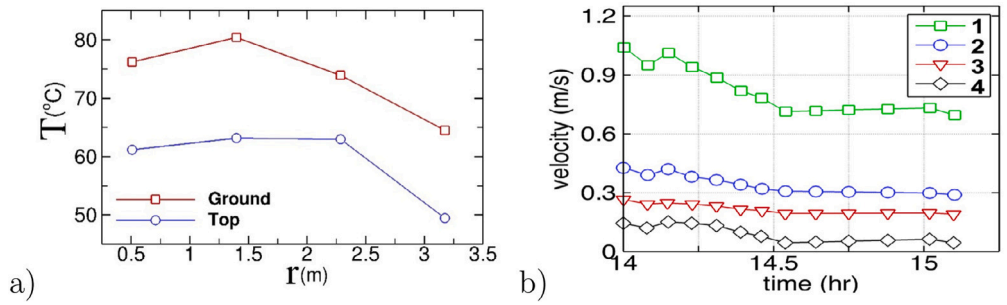

Fig. 4. (a) Temperature measurements at the collector bottom (ground) and cover (top), and (b) maximum radial velocity at different locations inside the collector versus time for June 14, 2019.
Source: Reprinted from Bahrainirad et al. (2020).

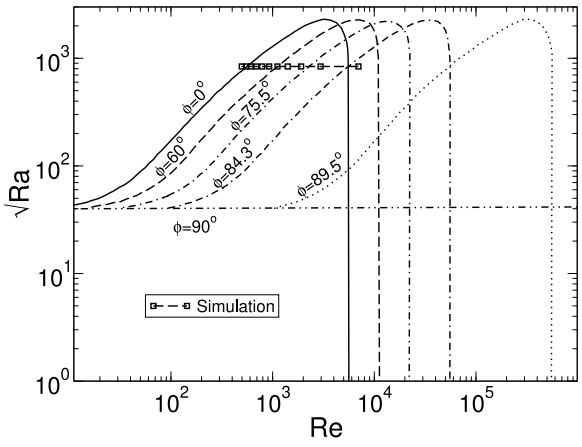

Fig. 5. Conditions for experiment and simulation (symbols) and neutral curves for plane RBP flow by Gage and Reid (1968).

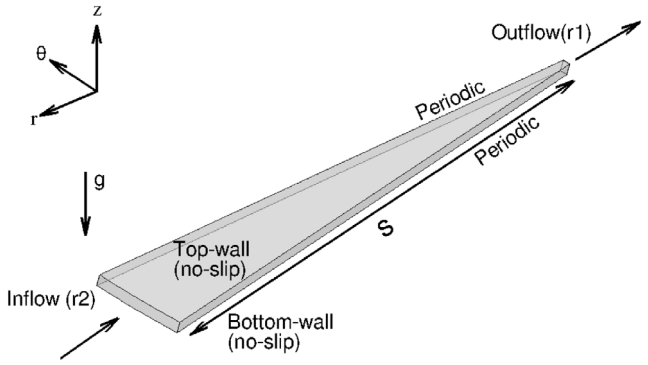

Fig. 6. Computational domain.

velocity profile was prescribed and a non-reflecting boundary condition based on Riemann invariants (Carlson, 2011) was applied. A characteristics-based boundary condition was employed at the outflow boundary (Gross and Fasel, 2007). Periodicity conditions were implicitly enforced in the azimuthal direction. Additional details on the discretization and boundary conditions can be found in Hasan and Gross (2021a,b).

4.2. Computational domain

The computational domain was the shape of a slice of a circular pie with an opening angle of $\Theta = 7.5$ degrees (Fig. 6). The inflow radius was placed at $r_1 = 125$ and the outflow radius was set to $r_2 = 10$, which corresponds to 0.33 m. The outflow radius is thus downstream of the thermocouple 1 location in Fig. 2c. In the wall-normal direction, grid points were clustered near the top and bottom wall based on an analytical function from Hasan and Gross (2021b). The total number of grid points in the wall-normal direction was $jx = 64$ and the same as in the earlier LES by Fasel et al. (2013). The grid points in the radial direction and the collocation points in the azimuthal direction were equidistantly spaced. A total of $ix = 512$ grid points were used in the radial direction (double the number of grid points compared to the earlier LES by Fasel et al. (2013)). The total number of Fourier modes in the azimuthal direction was $kx = 32$.

4.3. Procedure for numerical stability analysis

Numerical stability investigations are an alternative to linear stability theory (LST) investigations. In situations where the flow field or the flow physics are very complex, the latter approach is often not feasible and numerical stability investigations are the only option. For both approaches, first a steady basic flow has to be computed. Towards that end, a 2-D simulation with $kx = 0$ (only cosine mode in azimuthal direction) was carried out. The simulation was advanced in time until the changes (from timestep to timestep) of all flow quantities dropped to machine zero. For the numerical stability investigation, the basic flow was then extended in the azimuthal direction by adding additional Fourier modes that were initialized to zero. Then, random unsteady disturbances were generated with the FORTRAN subroutine "random_number" and added to all inflow velocity components. Thereby, a wide range of streamwise and azimuthal wavenumbers with a broad frequency spectrum was "excited". The maximum amplitude of the inflow disturbances was set to 10^{-6} to keep the disturbances small enough (i.e. linear) throughout the domain. Unsteady flow data were then recorded every 500 timesteps over a time interval of 153.6. The computational timestep for the simulation was $\Delta t = 0.0003$.

The recorded unsteady flow data were Fourier-transformed in time and in the azimuthal direction and the amplitudes, growth rates, phase speeds, and wave angles of the disturbance waves were computed. In accordance with LST, a wave ansatz is made for the disturbances,

$$u'(s,z,\theta,t) = \sum \hat{u}(z) e^{i(\alpha s + \beta\theta - \omega t)}, \tag{8}$$

where $s = r_2 - r$ is the streamwise coordinate measured from the inflow radius, r_2. The inflow boundary is at $s = 0$ and the outflow boundary is at $s = 115$. The mode shapes, which are referred to as eigenfunctions in LST, are denoted by $\hat{u}(z)$ where z is the wall-normal coordinate. Furthermore, $\alpha = \alpha_r + i\alpha_i$, β, and ω are the radial wavenumber, azimuthal wavenumber, and angular frequency, respectively. For $\alpha_i < 0$, the disturbance amplitudes grow in the streamwise direction. The radial and azimuthal wavelengths, λ_r and λ_θ, are related to the radial and azimuthal wavenumbers via $\alpha_r = 2\pi/\lambda_r$ and $\beta = 2\pi/\lambda_\theta = 2\pi k/(r\Theta)$ where k is the azimuthal mode number.

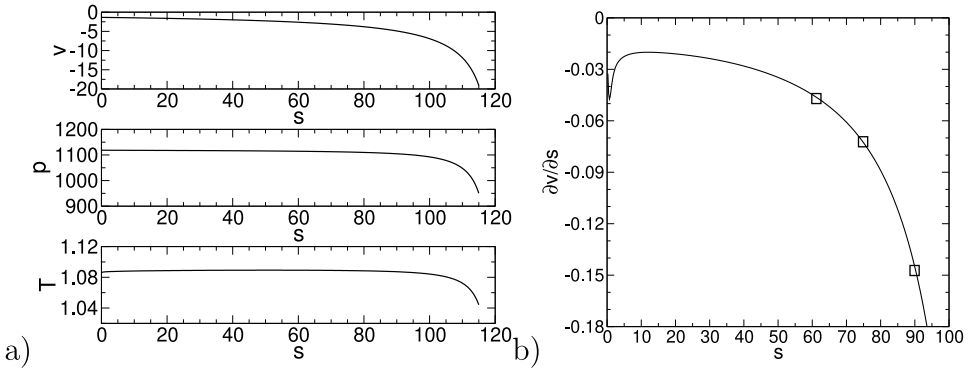

Fig. 7. (a) Average radial velocity, pressure and temperature versus streamwise coordinate. b) Radial acceleration (symbols are locations for analyses in Figs. 9b and 10).

The amplitude, A, and phase, ψ of the right- and left- traveling waves are obtained from the double Fourier transforms. The spatial growth rates are computed from

$$\alpha_i = -\frac{\partial \ln A}{\partial s}, \tag{9}$$

and the streamwise phase speeds are obtained from

$$c_s = -\frac{\frac{\partial \psi}{\partial t}}{\frac{\partial \psi}{\partial s}} = \frac{\omega}{\alpha_r}. \tag{10}$$

The phase speed in the wave propagation is

$$c = \frac{\omega}{\sqrt{\alpha_r^2 + \beta^2}} \tag{11}$$

with $\alpha_r = \omega / c_s$. The wave angle is related to the radial and azimuthal wavenumber via

$$\phi = \tan^{-1} \frac{\beta}{\alpha_r}. \tag{12}$$

More details regarding the code and the wave analysis can be found in Hasan and Gross (2021b).

4.4. Two-dimensional basic flow

The 2-D basic flow is discussed first as it provides the basis for the numerical stability investigation. In Fig. 7a the dimensionless average radial velocity, pressure and temperature are plotted versus the streamwise coordinate. As already discussed, the velocity displays an almost hyperbolic relationship on the radius. The pressure and temperature drop mildly towards the collector outflow. The streamwise decrease in temperature was also observed in the experiment as seen in Fig. 4a. From Fig. 4b it is noticed that the radial velocity increases substantially as the flow travels from the collector inflow (s4) to the chimney entrance (s1). In Fig. 7b the streamwise acceleration is plotted versus the streamwise coordinate. The radial acceleration increases strongly (i.e., becomes more negative) as the outflow is approached.

Profiles of the radial velocity and temperature for three different downstream locations, s = 61.094, 74.57, and 90.293, are provided in Fig. 8. The velocity profile at s = 61.094 is nearly parabolic. As the outflow is approached, the flow accelerates strongly and the profiles become fuller (e.g. s = 90.293). The slight asymmetry of the velocity profiles can be explained by the asymmetric heating and resulting asymmetric viscosity distribution. The temperature profiles are almost linear for all three locations (Fig. 8).

4.5. Three-dimensional flow

Instantaneous visualizations of the 3-D flow in Fig. 9 reveal longitudinal waves (wave angle of 90 deg). Shown on the left are contours of the instantaneous azimuthal velocity at the mid-collector height.

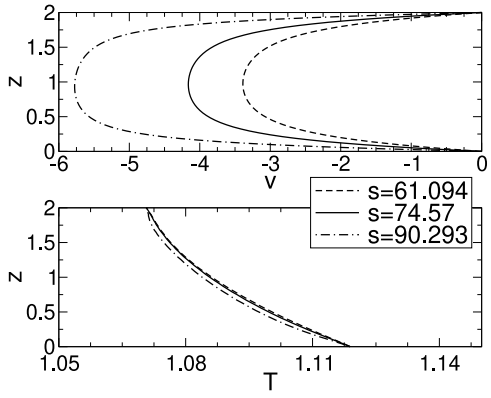

Fig. 8. Profiles of radial velocity and temperature.

The steady longitudinal waves appear to merge in the downstream direction (indicated by circles in Fig. 9a). This phenomenon is not observed for plane RBP flow. The “mergings” of steady waves occur because for a given azimuthal arc-length, only integer multiples of the azimuthal wavelength are possible (Hasan and Gross, 2021b). In Fig. 9b instantaneous azimuthal velocity contours are shown for three different streamwise locations (s = 74.57, 90.293, and 103.77). According to Fig. 9b, the amplitudes of the steady 3-D waves increase in the downstream direction.

In Fig. 10 contours of the spatial growth rate, α_i, for the same three streamwise locations are plotted over the azimuthal wavenumber, β, and frequency, ω. The total non-dimensional simulation time, T^* = 153.6 sets the lowest frequency, $\omega = 2\pi/T^* = 0.0409$. The shortest period is equal to two times the interval that the unsteady flow data was saved at, $2 \times 500 \times \Delta t = 0.3$. The corresponding maximum angular frequency is $\omega = 20.9$. Because of the low amplitudes and weak amplification for disturbance waves with $\omega > 10$, the growth rates above this frequency are very noisy. At s = 61.094 (Re = 974), the steady azimuthal waves (ω = 0) exhibit the highest growth rates. As the outflow is approached, the Reynolds number increases to 1,236 (s = 74.57) and 1,806 (s = 90.293) but remains below the critical Reynolds number for T-S instability to occur in plane channel flow, Re_c = 5400. The strong streamwise acceleration results in an attenuation of the disturbance growth rates. This finding is in agreement with stability investigations for accelerated boundary layer flows (Reed et al., 1996) and related stability simulations for radial RBP flow (Hasan and Gross, 2021b). The azimuthal wavenumber for the most amplified steady waves is $\beta \approx \pm 4.2$ for all three locations. This wavenumber corresponds to an azimuthal wavelength of 1.5 based on the collector half-height. Unsteady oblique waves with $\omega > 0$ are also amplified but their amplification rates are generally lower than those for the steady waves. The growth rates

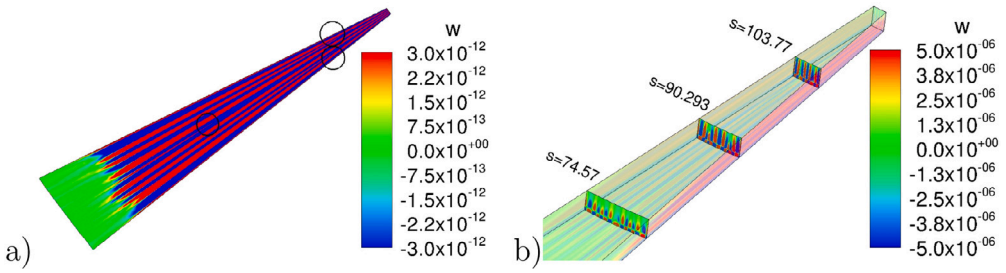

Fig. 9. Instantaneous azimuthal velocity contours (a) at mid-collector height and (b) for planes of constant radius.

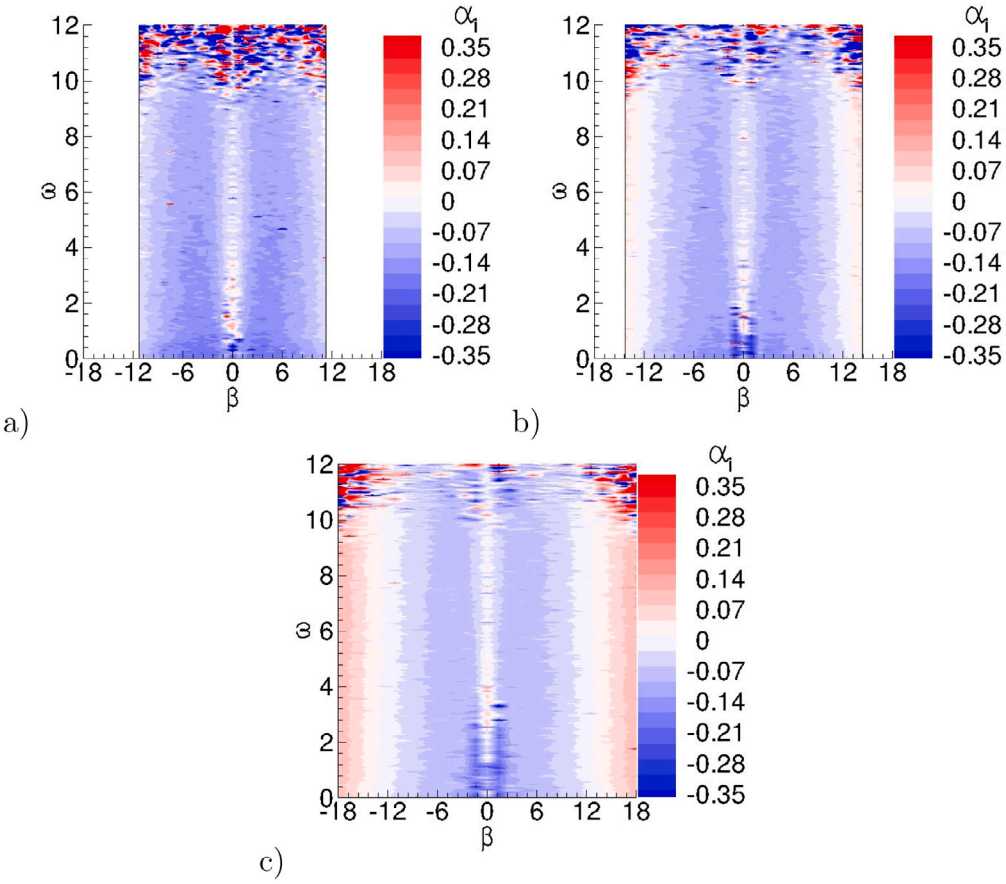

Fig. 10. Contours of spatial growth rate for (a) $s = 61.094$, (b) $s = 74.57$, and (c) $s = 90.293$.

for the right- and left-traveling oblique waves ("$+\beta$" and "$-\beta$") are nearly identical and decrease with increasing frequency which was also noticed for plane RBP flow (Hasan and Gross, 2021a). Overall, these findings are in qualitative agreement with the stability analysis by Gage and Reid (1968).

The growth rates of the left- and right-traveling oblique waves with $\beta = \pm 4.52$ are compared for $s = 61.094$ in Fig. 11a. In Fig. 11a, the gray lines represent raw data, colored lines are filtered data and the label "L" indicates linear regressions. The growth rates of the left- and right-traveling waves decrease with frequency and are almost identical. In Fig. 11b, the growth rates for $\omega = 0$ and $\omega = 1.0225$ are compared. In this figure "L" and "R" represent the left- and right-traveling waves and the symbols represent polynomial fits for $\omega = 1.0225$ (the dotted and dashed lines are the raw data). For both frequencies, steady disturbance waves with an azimuthal wavenumber of $\beta \approx \pm 4.2$ attain the highest growth rate (most negative α_i). The growth rates of the oblique waves with $\omega = 1.0225$ are lower (less negative α_i) than those of the steady waves.

The spatial growth rates of the steady waves for modes $k = 3 \ldots 7$ were plotted versus the streamwise acceleration (Fig. 12). Near the inflow, the acceleration is low ($\partial v/\partial s = -0.03$) and the higher mode numbers (such as $k = 7, 6$) are more amplified with growth rates close to $\alpha_i = -0.24$ (Fig. 12). As the outflow is approached, the lower mode numbers are more amplified, the streamwise acceleration is substantial ($\partial v/\partial s = -0.15$), and the maximum growth rates are reduced by up to 70% compared to the inflow. This confirms the stabilizing effect of the streamwise acceleration of the flow towards the outlet. The shift from the higher to the lower mode numbers can be explained by the constant azimuthal wavenumber of the most amplified waves ($\beta \approx \pm 4.2$) and the reduction of the circumference as the outflow is approached.

For plane RBP flow, the phase speeds increase and the wave angles decrease with increasing frequency (Hasan and Gross, 2021a). For the present radial RBP flow, the phase speeds of the left- and right-traveling oblique waves for $\beta = \pm 4.52$ and $\beta = \pm 6.78$ are plotted versus the frequency for $s = 61.094$ in Fig. 13a. The steady waves have a phase speed of zero. The phase speeds of the left- and right-traveling oblique

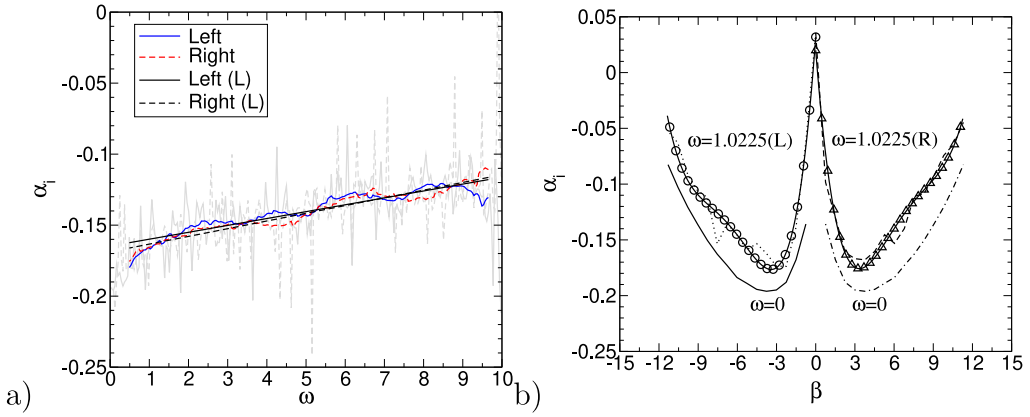

Fig. 11. Spatial growth rates at $s = 61.094$ versus (a) frequency for $\beta \approx \pm 4.52$ and (b) azimuthal wavenumber.
Source: Data extracted from Fig. 10a).

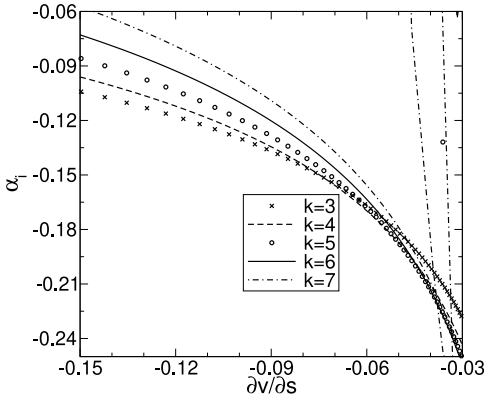

Fig. 12. Spatial growth rates for steady waves.

waves are identical and increase with frequency. For the same radial location, in Fig. 13b the phase speeds for $\omega = 1.0225$ and $\omega = 2.045$ are plotted versus the azimuthal wavenumber. The phase speeds of the left- and right-traveling waves decrease with increasing azimuthal wavenumber.

In Fig. 14a the wave angles for $\beta = \pm 4.52 \& \beta = \pm 6.78$ are plotted versus frequency and in Fig. 14b the wave angles for $\omega = 1.0225 \& \omega = 2.045$ are graphed over the azimuthal wavenumber. As can be observed, the wave angles of both the left- and right-traveling oblique waves decrease with frequency and increase with azimuthal wavenumber.

Iso-contours of the wall-normal disturbance velocity for the steady azimuthal mode with $k = 4$ at the collector mid-height are plotted in Fig. 15a. The wave fronts are aligned in the streamwise direction and the amplitude of the waves increases towards the outflow. The amplitudes of the steady ($\omega = 0$) and oblique waves ($\omega = \pm 2.045$) for the azimuthal wavenumber $k = 4$ are plotted versus the streamwise coordinate in Fig. 15b. The amplitude growth is initially nearly exponential (linear in log-plot) but then drops off sharply as the flow accelerates towards the outflow. For $s > 110$ the mode amplitudes level off indicating that the disturbance waves are no longer amplified. Overall, the steady longitudinal waves experience consistently stronger spatial growth than the oblique waves. It can be conjectured that the initial disturbance amplitudes for the 1:30 scale SCPP experiment are similar (i.e., low-amplitude random disturbances; no waves are favored) and that the steady longitudinal waves reach nonlinear amplitudes first. Based on the scaling analysis in Section 2 (Table 2), the turbulent Rayleigh number for the 1:30 scale and full-size SCPP are similar. This suggests that longitudinal coherent flow structures are to be expected for full-size SCPPs.

5. Conclusions

The flow inside the collector of solar chimney power plants (SCPPs) represents an inward radial Rayleigh-Bénard-Poiseuille (RBP) flow. Plane RBP flows are known to be subject to both buoyancy and viscosity-driven instabilities. Such instabilities, which also occur for radial RBP flows, can lead to the generation of longitudinal and transverse flow structures. Continuity dictates a strong streamwise acceleration of the collector flow. As streamwise acceleration is known to be stabilizing, the stability behavior of the RBP flow in SCPP collectors is expected to be different from that of conventional plane RBP flows. In spite of the fact that many practical aspects of the flow inside the collector of SCPPs have been analyzed in great detail, to the authors best knowledge the hydrodynamic instability of the inward radial RBP flow in SCPPs has not been investigated.

Measurements inside the collector of a 1:30 scale model of the Manzanares SCPP prototype (Haaf et al., 1983; Haaf, 1984; Schlaich, 1995; Schlaich et al., 2005) at the University of Arizona provided the reference Reynolds and Rayleigh numbers as well as boundary conditions for a numerical instability investigation. According to the neutral curves for plane RBP flow by Gage and Reid (1968), the Rayleigh number is high enough for buoyancy-driven instability to occur and the Reynolds number near the outflow exceeds the critical Reynolds number for viscosity-driven (Tollmien-Schlichting) instability in plane channel flow. In the simulation, randomized unsteady velocity disturbances were introduced at the collector inflow and the downstream evolution of the resulting disturbance waves was analyzed. Steady longitudinal waves were found to be most amplified. An apparent merging of the steady waves was explained by the fact that only integer multiples of the azimuthal wavenumber are possible. The most amplified azimuthal wavelength was found to be approximately 1.5 based on the collector half-height and remains nearly constant throughout the collector. Similar to plane RBP flow, oblique waves are also amplified in the collector. The growth rates of the left- and right-traveling oblique waves are nearly identical but lower than the growth rates of the steady waves. As a consequence of the strong streamwise acceleration, the growth rates of the steady three-dimensional and oblique waves are strongly attenuated towards the collector outflow.

A scaling analysis indicates that the present results are also relevant for full-size SCPPs. Instabilities of the laminar basic flow at the lower Rayleigh and Reynolds number of the 1:30 model experiment will likely translate to instabilities of the turbulent basic flow for the much larger Rayleigh and Reynolds numbers of full-size SCPPs. The present stability investigation is unique and indicates that Therefore, based on the present analysis, streamwise coherent flow structures are expected for the collector of full-size SCPPs. The flow structures will enhance the wall-normal momentum and heat transfer and increase the streamwise

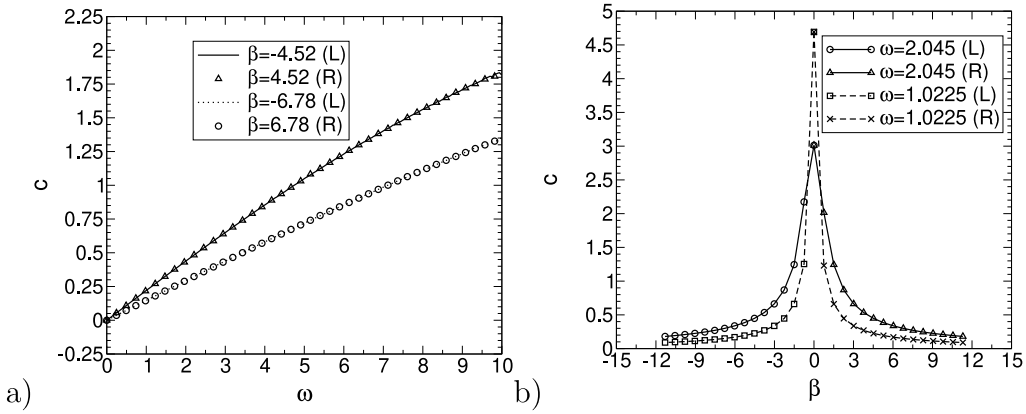

Fig. 13. Phase speed at $s = 61.094$ versus (a) frequency and (b) azimuthal wavenumber.

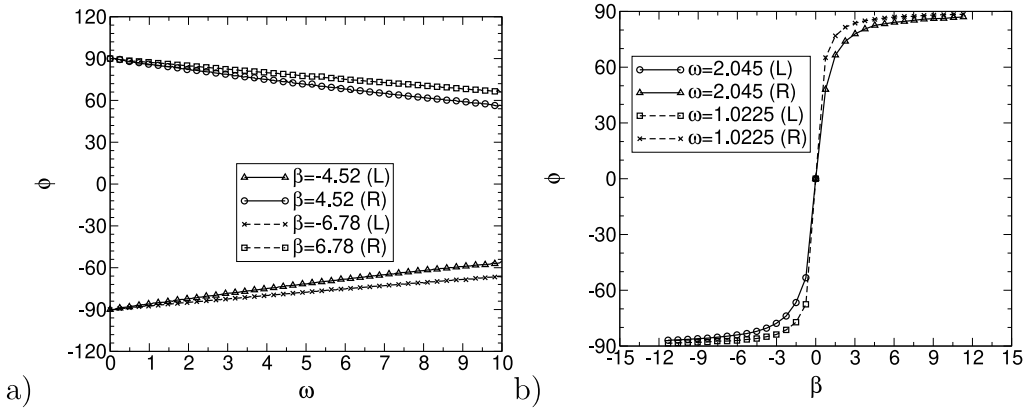

Fig. 14. Wave angle at $s = 61.094$ versus (a) frequency and (b) versus azimuthal wavenumber.

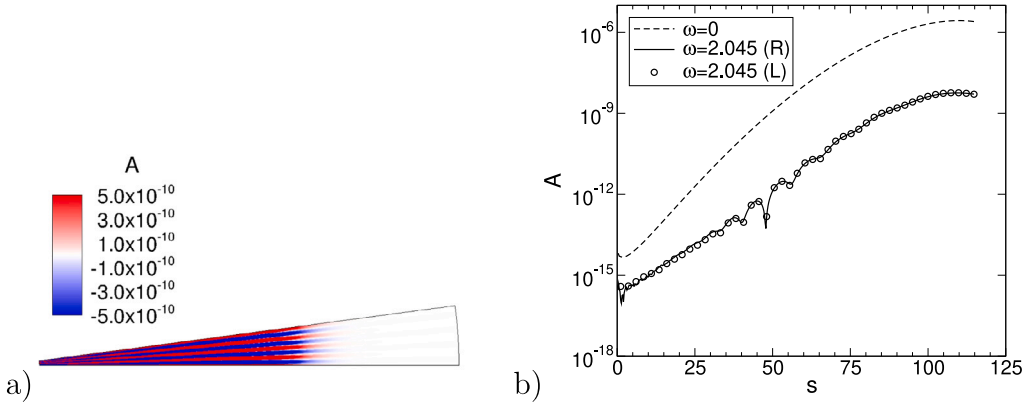

Fig. 15. (a) Iso-contours of wall-normal disturbance amplitude at channel mid-height for steady waves ($\omega = 0$) and (b) mode amplitudes versus streamwise coordinate for $k = 4$.

total pressure loss in the collector. The quantitative investigation of the effect of collector flow instabilities and resulting coherent flow structures on important SCPP performance parameters will be subject of future research.

Declaration of competing interest

The authors declare that they have no known competing financial interests or personal relationships that could have appeared to influence the work reported in this paper.

Acknowledgments

This material is based upon work supported by the National Science Foundation, USA under grant no. 1510179 and 1510717 with Dr. Ronald Joslin serving as program manager.

References

Ayadi, A., Driss, Z., Bouabidi, A., Abid, M.S., 2017. Experimental and numerical study of the impact of the collector roof inclination on the performance of a solar chimney power plant. Energy Build. 139, 263–276.

Ayadi, A., Driss, Z., Bouabidi, A., Nasraoui, H., Bsisa, M., Abid, M.S., 2018. A computational and an experimental study on the effect of the chimney height on

the thermal characteristics of a solar chimney power plant. Proc. Inst. Mech. Eng. E 232, 503–516.
Backström, T.W.V., Fluri, T.P., 2006. Maximum fluid power condition in solar chimney power plants – An analytical approach. Sol. Energy 80, 1417–1423.
Bahrainirad, L., Hasan, M.K., Fasel, H.F., Gross, A., 2020. Experimental and numerical investigation of a roof-scale solar chimney. In: AIAA 2020-0838, Florida, USA.
Balijepalli, R., Chandramohan, V.P., Kirankumar, K., 2020. Development of a small scale plant for a solar chimney power plant (SCPP): A detailed fabrication procedure, experiments and performance parameters evaluation. Renew. Energy 148, 247–260.
Bernardes, M.A.D.S., 2017. Preliminary stability analysis of the convective symmetric converging flow between two nearly parallel stationary disks similar to a Solar Updraft Power Plant collector. Sol. Energy 141, 297–302.
Bernardes, M.A.D.S., Valle, R.M., Cortez, M.F.B., 1999. Numerical analysis of natural laminar convection in a radial solar heater. Int. J. Therm. Sci. 38, 42–50.
Bernardes, M.A.D.S., Vob, A., Weinrebe, G., 2003. Thermal and technical analyses of solar chimneys. Sol. Energy 75, 511–524.
Carlson, J.R., 2011. Inflow/outflow boundary conditions with application to FUN3D. Report No. NASA/TM-2011-217181 (NASA Center for AeroSpace Information, Hanover, MD).
Chang, M.Y., Lin, T.F., 1998. Experimental study of aspect ratio effects on longitudinal vortex flow in mixed convection of air in a horizontal rectangular duct. Int. J. Heat Mass Transfer 41, 719–733.
Chang, M.Y., Yu, C.H., Lin, T.F., 1997. Changes of longitudinal vortex roll structure in a mixed convective air flow through a horizontal plane channel: an experimental study. Int. J. Heat Mass Transfer 40, 347–363.
Fallah, S.H., Valipour, M.S., 2019. Evaluation of solar chimney power plant performance: The effect of artificial roughness of collector. Sol. Energy 188, 175–184.
Fan, P., 2016. The standard upwind compact difference schemes for incompressible flow simulations. J. Comput. Phys. 322, 74–112.
Fasel, H.F., Meng, F., Gross, A., 2015. Numerical and experimental investigation of 1:33 scale solar chimney power plant. In: 11th International Conference on Heat Transfer, Fluid Mechanics, and Thermodynamics, South Africa.
Fasel, H.F., Meng, F., Shams, E., Gross, A., 2013. CFD analysis for solar chimney power plants. Sol. Energy 98 Part A, 12–22.
Fyfe, D.J., 1966. Economical evaluation of Runge-Kutta formulae. J. Comput. Phys. 20, 392–398.
Gage, K.S., Reid, W.H., 1968. The stability of thermally stratified plane Poiseuille flow. J. Fluid Mech. 33, 21–32.
Gentry, M.C., Jacobi, A.M., 2002. Heat transfer enhancement by delta-wing-generated tip vortices in flat-plate and developing channel flows. J. Heat Transfer 124, 1158–1168.
Gross, A., Fasel, H.F., 2007. Characteristic ghost cell boundary condition. AIAA J. 45, 302–306.
Guo, P., Li, J., Wang, Y., Liu, Y., 2013. Numerical analysis of the optimal turbine pressure drop ratio in a solar chimney power plant. Sol. Energy 98, 42–48.
Haaf, W., 1984. Solar chimneys part II: Preliminary test results from the Manzanares pilot plant. Int. J. Sol. Energy 2, 141–161.
Haaf, W., Friedrich, K., Mayr, G., Schlaich, J., 1983. Solar chimneys part I: Principle and construction of the pilot plant in manzanares. Int. J. Sol. Energy 2, 3–20.
Hasan, M.K., Gross, A., 2020. Temporal secondary stability simulation of Rayleigh-Beńard-Poiseuille flow. Int. J. Heat Mass Transfer 159, 120098 (1–12).
Hasan, M.K., Gross, A., 2021a. Higher-order-accurate numerical method for temporal stability simulations of Rayleigh-Beńard-Poiseuille flows. Internat. J. Numer. Methods Fluids 93, 127–147.
Hasan, M.K., Gross, A., 2021b. Numerical instability investigation of inward radial Rayleigh-Bénard-Poiseuille flow. Phys. Fluids 33, 034120 (1–16).
Hu, S., Leung, D.Y.C., Chan, J.C.Y., 2017. Impact of the geometry of divergent chimneys on the power output of a solar chimney power plant. Energy 120, 1–11.
Khidhir, D.K., Atrooshi, S.A., 2020. Investigation of thermal concentration effect in a modified solar chimney. Sol. Energy 206, 799–815.
Koonsrisuk, A., Chitsomboon, T., 2013. Effects of flow area changes on the potential of solar chimney power plants. Energy 51, 400–406.
Luijkx, J.M., Platten, J.K., Legros, J.C., 1981. On the existence of thermoconvective rolls, transverse to a superimposed mean Poiseuille flow. Int. J. Heat Mass Transfer 24, 1287–1291.
Masters, G.M., 2004. Renewable and Efficient Electric Power Systems. John Wiley and Sons, Hoboken, NJ.
Ming, T.Z., Liu, W., Pan, Y., Xu, G., 2008. Numerical analysis of flow and heat transfer characteristics in solar chimney power plant with energy storage layers. Energy Convers. Manage. 49, 2872–2879.
Ming, T., Liu, W., Xu, G., 2006. Analytical and numerical investigation of the solar chimney power plant systems. Int. J. Energy Res. 30, 861–873.
Ming, T., Wang, X., de Richter, R.K., Liu, W., Wu, T., Pan, Y., 2012. Numerical analysis on the influence of ambient crosswind on the performance of solar updraft power plant system. Renew. Sustain. Energy Rev. 16, 5567–5583.
Nasraoui, H., Driss, Z., Ayedi, A., Kchaou, H., 2019. Numerical and experimental study of the aerothermal characteristics in solar chimney power plant with hyperbolic chimney shape. Arab. J. Sci. Eng. 44, 7491–7504.
Nizetic, S., Klarin, B., 2010. A simplified analytical approach for evaluation of the optimal ratio of pressure drop across the turbine in solar chimney power plants. Appl. Energy 87, 587–591.
Ouazzani, M.T., Platten, J.K., Mojtabi, A., 1990. Etude expérimentale de la convection mixte entre deux plans horizontaux à températures différentes-II. Int. J. Heat Mass Transfer 33, 1417–1427.
Pastohr, H., Kornadt, O., Gurlebeck, K., 2004. Numerical and analytical calculations of the temperature and flow field in the upwind power plant. Int. J. Energy Res. 28, 495–510.
Pearlstein, A.J., 1985. On the two-dimensionality of the critical disturbances for stratified viscous plane parallel shear flows. Phys. Fluids 28, 751–753.
Reed, H.L., Saric, W.S., Arnal, D., 1996. Linear stability theory applied to boundary layers. Annu. Rev. Fluid Mech. 28, 389–428.
Schlaich, J., 1995. The Solar Chimney: electricity from the Sun. Edition Axel Menges.
Schlaich, J., Bergermann, R., Schiel, W., Weinerbe, G., 2005. Design of commercial solar updraft tower systems-utilization of solar induced convective flows for power generation. J. Solar Energy Eng. 127, 117–124.
Shukla, R.K., Tatineni, M., Zhong, X., 2007. Very high-order compact finite difference schemes on non-uniform grids for incompressible Navier-Stokes equations. J. Comput. Phys. 224, 1064–1094.
Van Santen, H., Kleijn, C.R., Van Den Akker, H.E.A., 2000. Mixed convection in radial flow between horizontal plates-I. Numerical simulations. Int. J. Heat Mass Transfer 43, 1523–1535.
Van Santen, H., Kleijn, C.R., Van Den Akker, H.E.A., 2020. Mixed convection in radial flow between horizontal plates-II. Experiments. Int. J. Heat Mass Transfer 43, 1537–1546.
Xu, G., Ming, T., Pan, Y., Meng, F., Zhou, C., 2011. Numerical analysis on the performance of solar chimney power plant system. Energy Convers. Manage. 52, 876–883.